

This item is the archived peer-reviewed author-version of:

Ni cluster formation in low temperature annealed $Ni_{50.6}Ti_{49.4}$

Reference:

Pourbabak Saeid, Wang Xiebin, Van Dyck Dirk, Verlinden Bert, Schryvers Dominique.- Ni cluster formation in low temperature annealed $Ni_{50.6}Ti_{49.4}$
Functional materials letters - ISSN 1793-6047 - 10:1(2017), 1740005
Full text (Publisher's DOI): <https://doi.org/10.1142/S1793604717400057>
To cite this reference: <https://hdl.handle.net/10067/1425450151162165141>

Functional Materials Letters
Vol. 1, No. 1 (2015) Article number
©World Scientific Publishing Company

Ni cluster formation in low temperature annealed Ni_{50.6}Ti_{49.4}

Saeid Pourbabak^{*,†}, Xiebin Wang^{‡,§}, Dirk Van Dyck^{*}, Bert Verlinden[§], Dominique Schryvers^{*}

^{*}EMAT, University of Antwerp, Groenenborgerlaan 171, B-2020 Antwerp, Belgium

[§]MTM, Department of Materials Engineering, University of Leuven, Kasteelpark Arenberg 44, 3001 Leuven, Belgium

Received Day Month Year; Revised Day Month Year

Various low temperature treatments of Ni_{50.6}Ti_{49.4} have shown an unexpected effect on the martensitic start temperature. Periodic diffuse intensity distributions in reciprocal space indicate the formation of short pure Ni strings along the <111> directions in the B2 ordered lattice, precursing the formation of Ni₄Ti₃ precipitates formed at higher annealing temperatures.

Keywords: cluster model, diffuse intensity, short range order, precursor

1. Introduction

Ageing is an effective way to improve the shape memory and mechanical properties of Ni-rich Ni-Ti alloys due to the formation of Ni₄Ti₃ precipitates.^{1,2} It is well known that ageing leads to progressive precipitation with increasing ageing time, temperature and Ni content.³ The effect of intermediate temperature⁴⁻⁶ (670–1070 K) and low temperature^{1,7} (470–570 K) ageing on the transformation behavior have been widely investigated before. Ageing at temperatures below 470 K has been considered too low to cause precipitation, as reported by Kim and Miyazaki.¹ By transmission electron microscope (TEM), they did not observe any precipitates in a Ni_{50.9}Ti_{49.1} sample quenched from 1070 K and aged at 373 K for 3000h, and in the sample aged at 473 K tiny 2–3 nm precipitates were first observed after 100h. However, Kompatscher *et al.* reported that if the sample is quenched from higher temperature, *i.e.* 1270 K, small precipitates of size 1 nm can be detected by means of small-angle neutron scattering, even without ageing.⁸ Zheng *et al.* ascribed the suppression of the B2–B19' martensitic transformation (MT) in a sample aged below 600 K to the atomic rearrangement as a precursor phenomenon for precipitation.³ Kustov *et al.* observed that room temperature (RT) ageing combined with differential scanning calorimetry (DSC) cycles strongly suppresses the MT for a sample quenched from 1270 K, from which they

concluded the formation of nm size precipitates or their nuclei.⁹ Wang *et al.* performed a systematic investigation of a different set of samples to decouple the effect of DSC cycling and RT aging.¹⁰ They found that only RT aging has no detectable effect on the transformation, while RT aging after thermal cycling can substantially suppress the MT. In the present work the atomic scale structural changes of the latter experiment are investigated using different TEM techniques.

2. Experimental Procedure

2.1. Sample production and treatment

A Ni_{50.6}Ti_{49.4} alloy was annealed at 1273 K for 2 hours followed by room temperature water quenching (WQ). The quenched samples were subjected to 3 different procedures:

- Protocol A, 9 samples: DSC cycling was done on one sample immediately after quenching, the remaining 8 samples were aged at RT respectively for 1, 2, 4, 8, 15, 30, 60 and 90 days, always followed by a DSC cycle. All samples were again aged at RT until now (all experiments started in March 2015).
- Protocol B: 9 consecutive DSC cycles were performed on one sample immediately after quenching and followed by aging at RT until now.

[†] Email: saeid.pourbabak@uantwerpen.be

[‡] Currently at Key Laboratory for Liquid-Solid Structural Evolution and Processing of Materials, Ministry of Education, Shandong University, Jingshi Road 17923, Jinan 250061, P.R. China.

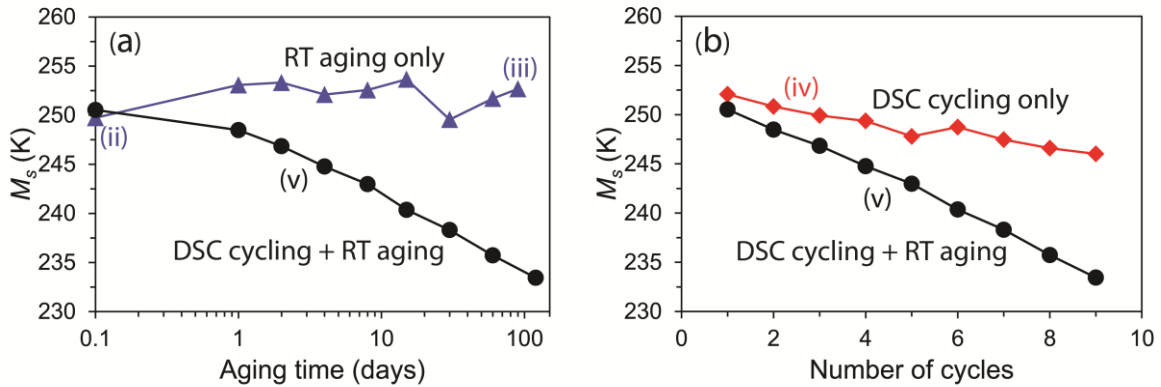


Fig 1 (a) M_s comparison between samples only aged at RT and sample aged at RT combined with DSC cycling; (b) M_s comparison between sample with consecutive DSC cycling and sample aged at RT combined with DSC cycling.

- Protocol C: 1 sample was measured by DSC cycling immediately after quenching and aged at RT until now, interrupted by single DSC cycles performed at 1, 2, 4, 8, 15, 30, 60 and 120 days after quenching.

The DSC measurements were performed between 123 and 298 K in a TA Q2000 calorimeter with a cooling/heating rate of 10 K min^{-1} .

The MT start temperature (M_s) versus aging time for protocols A and C is compared in Fig 1 (a). M_s of protocol A varies between 250 and 254 K, and does not seem to be affected by aging¹⁰. M_s of protocol C decreases from 250 K for the measurement just after quenching to 233 K after 120 days.

M_s versus number of thermal cycles for protocols B and C are shown in Fig 1 (b). M_s of the sample with only consecutive thermal cycling lowers from 252 to 246 K, but it is much less intense than that of the combined aging–cycling treatment.

2.2. TEM

Five samples with the following treatment were selected for the TEM investigation:

- 2Hr1270K+WQ+ag@RT
- 2Hr1270K+WQ+1DSC+ag@RT (protocol A)
- 2Hr1270K+WQ+ag90days@RT+1DSC+ag@RT (protocol A)
- 2Hr1270K+WQ+9DSC+ag@RT (protocol B)
- 2Hr1270K+WQ+1DSC @ 0,1,2,4,8,15,30,60,120 days and ag@RT in between+ag@RT (protocol C)

The corresponding M_s points of samples (ii) and (iii) are indicated on Fig 1 (a). Sample (iv) produces all points of the upper (red) curve in Fig 1 (b) and all points of the lower (black) graphs in Fig 1 (a) and (b) are obtained from sample (v). Sample (i) had no DSC cycle and appears in none of the graphs.

Samples were cut into discs of 3 mm diameter and grinded to a thickness of $120 \mu\text{m}$ followed by electropolishing.¹¹ The obtained electron transparent specimens were used for high resolution TEM (HRTEM) and acquisition of electron diffraction patterns on a FEI Tecnai G2 instrument. Also high angle annular dark field scanning TEM (HAADF-STEM) on a FEI Titan 50–80 instrument operating at 300 kV was used to exploit the Z-contrast ability of the technique.

Tilt series of selected area electron diffraction (SAED) patterns were acquired to study the reciprocal space in three dimensions. Dedicated SAED patterns were also acquired in some different high and low order zones aiming for further quantification. In order to achieve comparable quantitative data some considerations were taken into account: Convergent beam electron diffraction (CBED) was applied to measure the sample thickness^{12,13} and use a consistent thickness for all acquisitions. Microscope settings such as beam spotsize, condenser and objective lenses excitation, condenser and selected area apertures and camera length were kept unchanged. Also camera settings (exposure time) and calibration (gain and bias corrections) were consistent for the whole procedure.

3. Results

Fig 2 (a) shows a bright field TEM image of sample (i) and in which clearly no fully formed precipitates can be seen. Accordingly, the SAED pattern of the zone $[012]_{B2}$ shown in Fig 2 (b) does not represent any of the characteristic superspots of Ni_4Ti_3 precipitates along $\langle 123 \rangle^*$. However, it does reveal a clear structured pattern of diffuse intensity. By tilting the sample it is found that similar diffuse intensity patterns also exist in zones in which no Ni_4Ti_3 superspots are expected in samples with fully grown precipitates, such as $[122]_{B2}$ shown in Fig 2 (c). The main properties of the

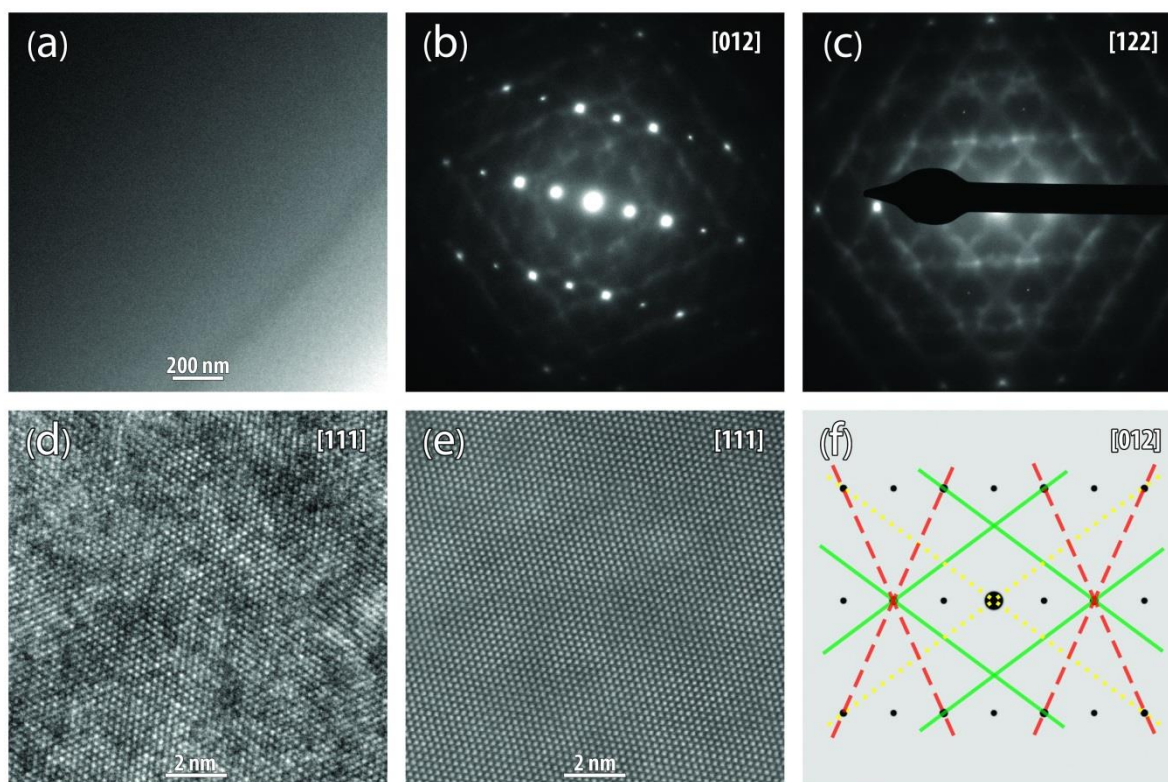


Fig 2 (a) Bright field; (b) [012] SAED pattern; (c) [122] SAED pattern; (d) HRTEM; (e) HAADF-STEM of sample (i); (f) intersection traces of $(012)^*$ and $\{111\}^*$ planes.

diffuse intensities observed in different zone axes may be expressed as follows:

- (i) they are more pronounced in high order zones and less visible in low order zones,
- (ii) they are arranged around specific geometrical loci,
- (iii) in the 2D SAED patterns they generally appear as line shapes,
- (iv) they reveal a periodical character.

Contrary to the clear structural diffuse intensity found in reciprocal space, which indicates the existence of some kind of short range order in the lattice, HRTEM images taken along various zones do not reveal any useful information. In Fig 2 (d) an example along the $\langle 111 \rangle_{B2}$ direction is shown which does reveal some contrast variation in the resolved atom columns. However, these contrast variations strongly depend on the used imaging focus and are thus not very reliable to be used as guidance for any possible structural feature, although they have been shown to provide some guidance in another system.^{14,15}

The HAADF-STEM image acquired along the same $\langle 111 \rangle_{B2}$ and shown in Fig 2 (e) is more stable against focal changes and is expected to reveal differences in the intensity of atom columns due to Z-contrast, in case changes in atom occupation along the columns exist.¹⁶ In the perfect austenite B2 matrix the $\langle 111 \rangle_{B2}$ atom columns consist of

alternating Ni and Ti atoms, so all dots in the HAADF-STEM image should have the same intensity. And since in the hexagonal Ni_4Ti_3 precipitates 1 out of 7 $\langle 001 \rangle_H // \langle 111 \rangle_{B2}$ columns of atoms is pure Ni, the diffuse intensity observed in the SAED patterns could indicate the existence of some precursors, *i.e.* increased Ni occupation along some $\langle 001 \rangle_H // \langle 111 \rangle_{B2}$ columns. For this reason one might expect to see some variation in the HAADF-STEM intensities. However, the measured intensity differences run up to about 8% while MULTTEM¹⁷ simulations indicate that a precursor of 7 unit cells (*i.e.*, 15 Ni atoms in a $\langle 111 \rangle_{B2}$ row) yields an intensity increment of only 2%. Thus, the observed difference in the HAADF-STEM intensity of atomic columns cannot be attributed to the presence of a precursor related to the reciprocal diffuse intensities.

A tilt series of SAED patterns is acquired to obtain a 3D view of the diffuse intensity in reciprocal space. This shows that the diffuse streaks observed in each diffraction pattern, to a first approximation, are created by the intersection of diffuse 2D $\{111\}^*_{B2}$ sheets with the observing plane. All four equivalent $\{111\}^*_{B2}$ families of parallel planes exist with only even values of h,k,l occurring.

There are two exceptions for the above statements, both concerning the absence of specific traces of $(111)^*$ planes. In Fig 2 (f) the loci of intersections of $\{111\}^*_{B2}$ planes with

the $(012)_{B_2}^*$ plane are schematically plotted. The dashed red streaks are obviously absent in Fig 2 (b). This phenomenon, where the traces of one or two $\{111\}_{B_2}^*$ families are absent, is observed in all diffraction patterns of the series. Investigating the properties of the invisible traces reveals that diffuse planes with angles smaller than about 48° with the viewing plane cannot be seen in the diffraction pattern. In the above example the angle of the green streaks is 75° , while that of the dashed red streaks is 39° . The same phenomenon was observed by Baba-Kishi *et al.* in PZT ceramics, while they found 67° as the critical angle.¹⁸ It is

still unclear whether this is related to the relative orientation of these families of $\{111\}_{B_2}^*$ planes to the selected zone or whether there is a structural origin. The reason for the absence of the dotted yellow streaks will be explained in the following section.

SAED patterns of all five samples were obtained in the same conditions as explained before. The results for the $[112]_{B_2}$ zone axis are presented in Fig 3. A slight difference in the intensity and distribution of the diffuse intensities can already be distinguished by eye. In order to allow quantitative comparison between the samples, a rectangle

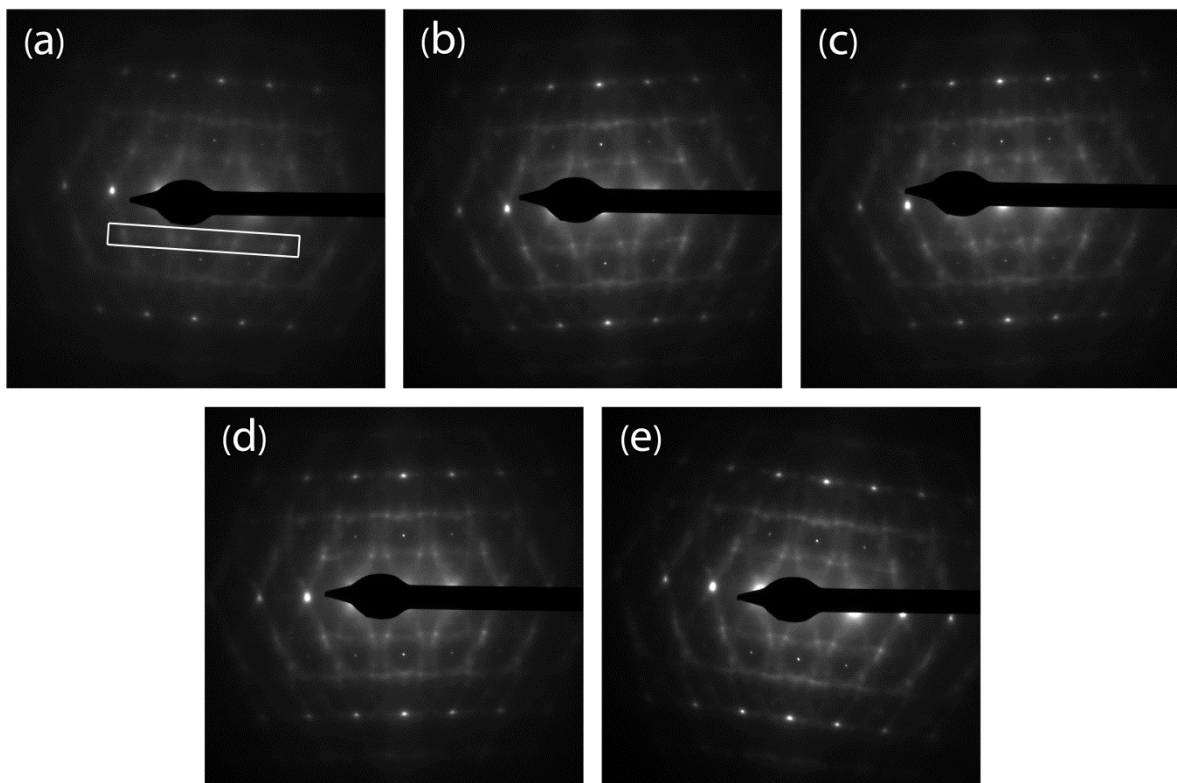


Fig 3 (a) to (e), $[112]_{B_2}$ SAED of samples (i) to (v). The rectangle shown in (a) indicates the area over which the averaging is performed.

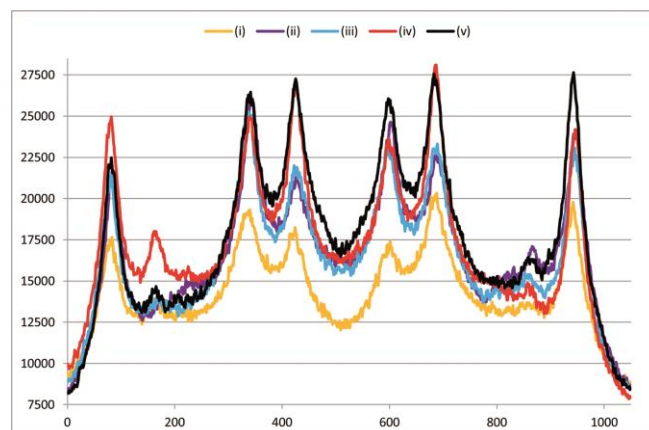


Fig 4 Rectangular averaged profiles of the same region in the $[112]_{B_2}$ SAED patterns of samples (i) to (v).

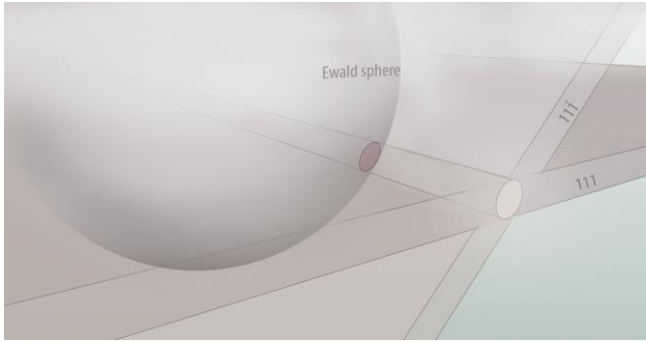


Fig 5 Schematic of the cross-section of the Ewald sphere with that of two $\{111\}^*$ diffuse planes, yielding a diffuse spot in the diffraction pattern.

region of the patterns as shown Fig 3 (a) was selected to achieve an averaged line profile. In this region 3 diffuse planes cross each other and the spot-like intensity enhancements correspond to the intersection of the Ewald sphere with the intersection line of two such diffuse planes, as schematically shown in Fig 5.

The rectangular profiles obtained from all SAEDs are plotted in Fig 4. The lowest (yellow) trace belongs to sample (i) with no DSC cycling. Samples (ii) (purple) and (iii) (blue) mostly show a very similar intensity distribution. This is also true for remaining (iv) (red) and (v) (black) samples. The average of the four middle peaks is compared with the central minimum for each graph to allow for a relative quantification. The results are presented in Table 1 where the ratio of maxima average and the minimum of sample (i) is taken as a reference. It is clear that the intensity of the diffuse spots increases with increasing treatment times, even at those very low temperatures.

Table 1 Statistical data of Fig 4

	Max avg.	min	Max avg. - min	%
(i)	18763	12176	6586	100
(ii)	23489	15958	7531	114
(iii)	23451	15477	7973	121
(iv)	25644	15932	9712	147
(v)	26692	16691	10001	152

4. Discussion

In order to find the structural configurations underlying the diffuse intensities the Cluster Model¹⁹⁻²², which assigns the geometry of reciprocal diffuse intensity to that of microdomains in real space is used. The kinematical diffraction amplitude $A(\mathbf{k})$ can be written as:

$$A(\mathbf{k}) = \langle F(\mathbf{g}) \rangle \sum_i e^{2\pi i \mathbf{k} \cdot \mathbf{r}_i} + \sum_i \Delta F_i(\mathbf{k}) e^{2\pi i \mathbf{k} \cdot \mathbf{r}_i},$$

where \mathbf{k} is a general vector in reciprocal space, \mathbf{r}_i is the position of atom i in the unit cell, $\langle F(\mathbf{g}) \rangle$ is the average structure factor and $\Delta F_i(\mathbf{g})$ is the deviation of the local structure factor $F_i(\mathbf{g})$ from $\langle F(\mathbf{g}) \rangle$. The first term on the right yields the Bragg reflections and the second term describes the diffuse intensity. In a binary system with m_{Ni} and m_{Ti} the atomic fractions and f_{Ni} and f_{Ti} the scattering factors of Ni and Ti, respectively, $\Delta F_i(\mathbf{k})$ can be found as:

$$\Delta F_i(\mathbf{k}) = \begin{cases} m_{Ti} [f_{Ni}(\mathbf{k}) - f_{Ti}(\mathbf{k})] & Ni \text{ on position } i \\ -m_{Ni} [f_{Ti}(\mathbf{k}) - f_{Ti}(\mathbf{k})] & Ti \text{ on position } i \end{cases}$$

which by substituting the Flinn site occupation operator σ_i in the diffuse intensity term returns the diffuse amplitude as:

$$A^{(D)}(\mathbf{k}) = [f_{Ni}(\mathbf{g}) - f_{Ti}(\mathbf{g})] \sum_i \sigma_i e^{2\pi i \mathbf{k} \cdot \mathbf{r}_i}.$$

The normalized diffuse amplitude is then:

$$\hat{A}^{(D)}(\mathbf{k}) = \frac{A^{(D)}(\mathbf{k})}{f_{Ni}(\mathbf{g}) - f_{Ti}(\mathbf{g})} = \sum_i \sigma_i e^{2\pi i \mathbf{k} \cdot \mathbf{r}_i},$$

in which only the geometrical information on the position of atoms in σ_i is retained.

In cases in which the diffuse intensity is concentrated close to periodical loci in reciprocal space, more information can be obtained from the shape of the diffuse intensity loci. The loci with the translational symmetry in reciprocal space can be expressed as:

$$l(\mathbf{k}) = \sum_k \omega_k e^{2\pi i \mathbf{k} \cdot \mathbf{r}_k} = 0.$$

Assuming that all diffuse intensity is concentrated on the $l(\mathbf{k})$ loci we can write:

$$\hat{A}^{(D)}(\mathbf{k}) \cdot l(\mathbf{k}) = 0 \quad \text{for all } \mathbf{k}$$

which gives the ordering relation as follows:

$$\sum_k \omega_k \sigma_{j+k} = 0 \quad \text{for all } j$$

in which ω_k are coefficients of the Flinn operators. Considering even $\{111\}^*$ planes one finds $\sigma_1 = \sigma_2$, $\mathbf{r}_1 = [000]$ and $\mathbf{r}_2 = [\frac{1}{2}\frac{1}{2}\frac{1}{2}]$. This means that atoms occupying $[000]$ and $[\frac{1}{2}\frac{1}{2}\frac{1}{2}]$ positions are of the same kind, and since the alloy is slightly Ni-rich one can assume that having Ni in both sites is more favorable. In other words, the diffuse $\{111\}^*$ planes correspond with clusters of the form of pure Ni strings oriented along all four equivalent $\langle 111 \rangle_{B2}$ directions (as a reminder, in perfect ordered B2, the $\langle 111 \rangle_{B2}$ rows consist of alternating Ni and Ti atoms). As mentioned before, as far as the ordering is concerned, the Ni_4Ti_3 precipitates can be distinguished from the B2 structure since 1 out of 7 $[111]$ columns consists of pure Ni. This matches well with the

above clusters since these clusters in the quenched samples can be considered as early stages of some columns of the Ni_4Ti_3 precipitates which normally start appearing upon annealing. Having Ni atoms with the periodicity of $\frac{1}{2}\langle 111 \rangle$ also matches the $2\{111\}_{\text{B}2}$ periodicity of diffuse intensities in reciprocal space. The length of the clusters will inversely correspond with the width of the diffuse $\{111\}^*$ planes in reciprocal space and as long as the clusters do not get ordered (e.g., in an arrangement resembling the Ni_4Ti_3 structure) no intensity enhancement will exist inside the diffuse planes.

The missing dotted yellow streaks in Fig 2 (f) belong to the same family as the visible green streaks but pass through the central spot. This phenomenon was previously observed in Ti-Nb and explained by Sass.²³ The reason is that the scattering phase term is not changed by an atom shift normal to the reciprocal lattice vector. As the reciprocal lattice vector is passing through 000 and the atom columns are in the [111] direction, the scattering phase is the same before and after the formation of clusters and as a result a $\langle 111 \rangle$ cluster in the B2 structure will not produce a $\{111\}$ plane of diffuse intensity passing through 000.

Analyzing the data presented in Fig 2 (f) could possibly help explaining the effect of the DSC cycling on M_s . Sample (i) has the weakest concentration of diffuse intensity, which can be ascribed to very short clusters. The diffuse intensity is slightly more concentrated in samples (ii) and (iii), which both had only one DSC cycle but at different times during processing. The M_s of these two samples are also quite similar. The concentration of diffuse intensity is more pronounced in samples (iv) and (v) which had several DSC cycles. Sharper and more focused diffuse intensities in these cases can be explained by assuming more concentrated diffuse $\{111\}^*$ planes which leads to sharper cross-sections and thus stronger diffuse spots, e.g., as those highlighted in Fig 3. Such concentration of diffuse intensity can be related to the elongation of clusters which implies some short range diffusion or re-ordering of atoms during thermal cycling. However, since the cycling for the present samples was performed between 123 and 298 K, very little thermal energy is provided. Still, with a transformation front moving across the system, sufficient energy could be available on a local scale to move a single atom from one lattice site to the next²⁴. Since all of these samples still reveal strong diffuse intensity in the $[112]_{\text{B}2}$ zone in which no Ni_4Ti_3 superspots exist, no ordering into nano-precipitates is expected as yet, which is confirmed by the fact that no structural features can be recognized in the HRTEM or HAADF-STEM images. Whether or not the short pure Ni strings are at the origin of the decrease in M_s still needs to be elucidated.

5. Conclusions

The effect of low temperature thermal cycling combined with room temperature aging on the M_s of some $\text{Ni}_{50.6}\text{Ti}_{49.4}$ samples was investigated. Strong structured diffuse intensities condensed in periodic loci were observed in SAED. The cluster model was used to interpret the results which reveals the existence of microdomains in the form of clusters of pure Ni atoms along $\langle 111 \rangle_{\text{B}2}$ directions. Quantitative comparison between samples with and without a DSC cycle reveals that the more DSC cycles a sample has received, the more condensed the diffuse intensity which is expected to be caused by longer Ni clusters. The required energy for atom diffusion on a local scale may be provided by the transformation front moving across the system during the DSC cycling.

6. Acknowledgments

The authors like to thank the Flemish Science Foundation FWO for financial support under project G.0366.15N “Influence of nano- and microstructural features and defects in fine-grained Ni-Ti on the thermal and mechanical reversibility of the martensitic transformation and the shape memory and superelastic behavior”. We are also very grateful to Prof. Dr. Jan Van Humbeeck for initiating this work, for his continuous support and inspiring discussions.

7. References

- ¹ J.I. Kim and S. Miyazaki, *Acta Mater.* **53**, 4545 (2005).
- ² X. Wang *et al.*, *Acta Mater.* **82**, 224 (2015).
- ³ Y. Zheng *et al.*, *Acta Mater.* **56**, 736 (2008).
- ⁴ J. Khalil-Allafi, A. Dlouhy, and G. Eggeler, *Acta Mater.* **50**, 4255 (2002).
- ⁵ G. Fan *et al.*, *Acta Mater.* **52**, 4351 (2004).
- ⁶ B. Karbakhsh Ravari, S. Farjami, and M. Nishida, *Acta Mater.* **69**, 17 (2014).
- ⁷ Y. Zhou *et al.*, *Acta Mater.* **53**, 5365 (2005).
- ⁸ M. Kompatscher *et al.*, *Acta Mater.* **50**, 1581 (2002).
- ⁹ S. Kustov *et al.*, *Scr. Mater.* **103**, 10 (2015).
- ¹⁰ X. Wang *et al.*, *Scr. Mater.* **113**, 206 (2016).
- ¹¹ W. Tirry and D. Schryvers, *Mater. Sci. Eng. A* **481–482**, 420 (2008).
- ¹² I. Ackermann, *Ann. Phys.* **437**, 19 (1948).
- ¹³ P.M. Kelly *et al.*, *Phys. Status Solidi A* **31**, 771 (1975).
- ¹⁴ D. Schryvers, G. Van Tendeloo, and S. Amelinckx, *Mater. Res. Bull.* **20**, 361 (1985).
- ¹⁵ D. Schryvers and S. Amelinckx, *Acta Metall.* **34**, 43 (1986).
- ¹⁶ S.J. Pennycook and D.E. Jesson, *Ultramicroscopy* **37**, 14 (1991).
- ¹⁷ I. Lobato and D. Van Dyck, *Ultramicroscopy* **156**, 9 (2015).

¹⁸ K.Z. Baba-Kishi, T.R. Welberry, and R.L. Withers, *J. Appl. Crystallogr.* **41**, 930 (2008).

¹⁹ D. van Dyck *et al.*, *Phys. Status Solidi A* **43**, 541 (1977).

²⁰ R. de Ridder *et al.*, *Phys. Status Solidi A* **38**, 663 (1976).

²¹ R. de Ridder *et al.*, *Phys. Status Solidi A* **40**, 669 (1977).

²² D. van Dyck *et al.*, *Phys. Status Solidi A* **43**, 541 (1977).

²³ S.L. Sass, *J. Appl. Crystallogr.* **4**, 252 (1971).

²⁴ S. Kustov *et al.*, *Scr. Mater.* **123**, 166 (2016).

